KRONOS FUSION ENERGY

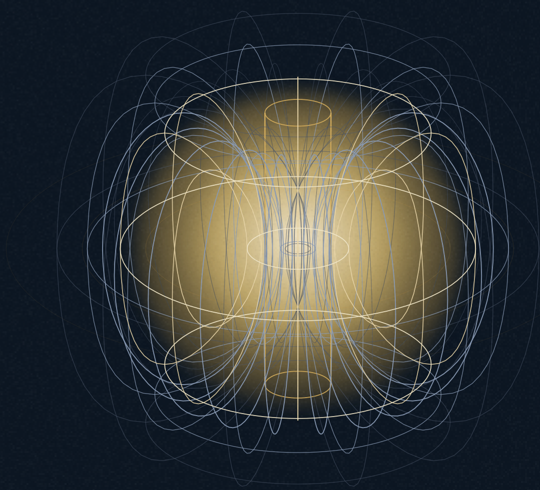

PAPER 2.30 · THE KRONOS 2026 SERIES

First-Wall and Plasma-Facing-Component Lifetime Under 14 MeV Loading: Displacement Damage, Bubble Swelling and Erosion in a Compact Spherical-Tokamak Breeder

Activation and waste classification tell you what a fusion structure becomes; they do not tell you how long it survives. We answer the survival question directly for the first…

Read it live — 3-D model · physics validator · film series

BY P I FORD AND G L KULCINSKI

2026 · EDITORIAL EDITION

THE OFFICIAL RECORD

What this document is, and how to read its numbers

This is a combined editorial. It gathers, in one volume, the two design studies Kronos Fusion Energy released in 2026 — a compact spherical-tokamak tritium/helium-3 breeder and a deuterium–helium-3 tandem-mirror generator — together with the intellectual-property estate, the people, and, in the internal edition, the full commercial case. The scientific text is the same text that appears in the arXiv preprints and the journal submissions; the editorial adds the apparatus a reader needs to hold the whole program at once, and nothing in the physics is altered to fit it.

THE HONESTY STANCE IS THE ASSET

Every headline quantity carries an **evidence class** — DERIVED RECOMPUTED MEASURED REQUIREMENT — and, where a number is a modelled extrapolation rather than a demonstrated value, it is labelled as such and its downside is shown next to it. Several quantities in the underlying corpus moved after first publication; where a value has been withdrawn or restated, the record says so plainly. This is deliberate: a diligence team will find the load-bearing assumptions, so the document surfaces them first.

TWO EDITIONS

This volume is issued in two editions. The **public edition** (light) carries the physics and the design only — no dollar, price, or per-kilogram figure appears anywhere in it. The **internal edition** (dark) adds the economics, the funding architecture, and the defense-commercial analysis, and is marked *Confidential* accordingly; it is not for public distribution. Where the commercial case rests on a modelled assumption rather than a demonstrated one, it is labelled as such and its downside is shown alongside it, on the same terms as the physics.

TITLE	The Kronos Fleet — Hyperion · Aegis · MetroVolt: A Combined Design & Commercialization Study
AUTHOR	Priyanca Ford, Founder & CEO, on behalf of Kronos Fusion Energy
EDITION	2026 Combined Editorial · first issue
COMPANION WORKS	The five-paper arXiv drop — (1) Breeder, (2) Burner, (3) REBCO magnet & tape, (4) Direct Energy Conversion, (5) AI/ML/Quantum control — with matching numbered Zenodo deposits, plus the IOP journal and IAEA-FEC submissions. Patents were filed before the drop.
NAMING	Hyperion = the breeder; Aegis (defense) and MetroVolt (data-center) = one generator in two housings. Internal mode letters (D1, L) do not appear on public surfaces.
STATUS	Conceptual design & simulation study. Nothing herein is a construction commitment.

HOW TO READ THIS VOLUME

The fleet at a glance, and the way its numbers are marked

This volume opens with *Orientation*, presents the five research papers as a bound sequence, and closes with the *Apparatus*. *Foundations* sets out the three general results both machines rest on. *Paper One* is the Hyperion breeder; *Paper Two* the Aegis / MetroVolt generator; *Papers Three, Four and Five* are the enabling science — high-field REBCO magnets and tape, direct energy conversion, and the AI / ML / quantum control stack. A *Digital Twin & 3-D Model* part follows, then the *Environmental* profile. The *Economics* and levelized cost and the *Business Case* and diligence record appear in the internal edition only; the *Simulations* proof record and the Apparatus — patent portfolio, team, limitations, and sources — close both editions.

THE FLEET AT A GLANCE

	HYPERION	AEGIS	METROVOLT
Role	Strategic-isotope foundry	Defense installation power	Campus power
Machine	**Spherical tokamak**	**Tandem mirror**	**Tandem mirror**
Fuel	Deuterium–tritium	Deuterium–helium-3	Deuterium–helium-3
Delivers	Tritium · ^{3}He · 14 MeV n	Resilient installation power	Firm campus power
Physics bar	**Fusion gain only**	Closure (gates named)	Closure + lunar ^{3}He
In the fleet	Breeds the fuel	Proves the generator	Commercial destination

HOW THE NUMBERS ARE MARKED

Every headline quantity carries an evidence class — DERIVED from first principles, RECOMPUTED from raw data, MEASURED in hardware, or a REQUIREMENT yet to be met. Financial figures carry a case label and are confined to the internal (confidential) edition. Values that moved after first publication are shown as withdrawn or restated rather than quietly changed. A capability you can evaluate is one whose limits are on the page.

ABSTRACT

First-Wall and Plasma-Facing-Component Lifetime Under 14 MeV Loading: Displacement Damage, Bubble Swelling and Erosion in a Compact Spherical-Tokamak Breeder

Activation and waste classification tell you what a fusion structure *becomes*; they do not tell you how long it *survives*. We answer the survival question directly for the first wall and plasma-facing components (PFCs) of the Hyperion compact spherical-tokamak breeder (design point $I_p = 9.66\,MA$, $Q = 3.076$, $P_{\text{fus}} = 85.04\,MW$, $P_n = 67.79\,MW$, neutron wall load $\Gamma_w = 1.885\,MW/m^2$, negative triangularity $\delta = -0.30$), computed on an independent, GPU-accelerated code stack rather than by literature scaling. Four coupled analyses set the lifetime. Displacement damage is computed from primary-knock-on-atom (PKA) recoil spectra folded to Norgett–Robinson–Torrens (NRT) displacements and corrected to surviving defects by athermal-recombination (arc-dpa) molecular dynamics, giving $18.85\,dpa/fpy$ at the bare wall and $9.78\,dpa/fpy$ in the reduced-activation ferritic-martensitic (RAFM) structure behind $3\,mm$ of tungsten armor. Transmutation (n, α) reactions co-produce helium at $\approx 12\,appm/dpa$ — an order of magnitude above any fission spectrum — which is why fission-irradiation data cannot be transferred and the lifetime must be set on the fusion spectrum. Rate-theory kinetics with a van der Waals bubble equation of state put the volumetric swelling at 0.024% (tungsten) and 0.017% (RAFM) at end-of-cycle dose, more than an order of magnitude below the 1–5% PFC design band. Binary-collision transport gives a peak deuterium-on-tungsten physical sputter yield of $1.35 \times 10^{-2}\,\text{atoms}\,\text{ion}^{-1}$ and sub-monolayer-per-pulse net erosion. Finite-element hydrogen transport gives a steady tritium permeation flux of $5.16e14\,/m^2s$ ($\approx 0.56\%$ of the implanted flux), a boundary condition for the fuel cycle rather than a life-limiter. The governing constraint is displacement-driven embrittlement: the wall is a scheduled-replacement component on a defined damage budget, with a service interval of order two full-power-years. Every headline number is a frozen anchor in the Kronos de-risking register (gates BR-L2-A24–A27).

Open-access deposit (code & data, CC BY 4.0): DOI 10.5281/zenodo.22645774 · Zenodo community *kronos_fusion_energy*. Explore it live: interactive 3-D model · physics validator.

Keywords: displacement damage · dpa · arc-dpa · helium embrittlement · bubble swelling · sputtering · tritium permeation · plasma-facing components · spherical-tokamak breeder

CONTENTS

Table of Contents

First-Wall and Plasma-Facing-Component Lifetime Under 14 MeV Loading: Displacement Damage, Bubble Swelling and Erosion in a Compact Spherical-Tokamak Breeder 3
Introduction 6
Governing equations and the formal lifetime problem 7
Computational methodology: the GPU-HPC campaign 11
Results 13
Discussion: comparison with published benchmarks 20
Limitations 21
Conclusion 22
References 27
One programme, many papers 31

NOMENCLATURE

Symbols, units, and the names of things

Q	plasma (fusion) gain, P_{fus}/P_{aux}
Q_E	engineering gain, net electric out / recirculating in
H_{98}	confinement enhancement over the IPB98(y,2) scaling
Z_{eff}	effective ion charge
c_{ee}	electron–electron bremsstrahlung leading coefficient, 2.120022 (exact)
τ_E	energy confinement time
I_p	plasma current
R_0, a	major radius, minor radius
κ, δ	elongation, triangularity
β_N	normalized plasma beta (Troyon-normalized)
TBR	tritium breeding ratio
DEC	direct energy conversion
CF	plant capacity factor (availability)
FOAK / NOAK / BOAK	first / n^{th} / best of a kind
Hyperion	the ST breeder (internal: Mode D2)
Aegis	the generator, defense/installation housing (internal: Mode M)
MetroVolt	the generator, data-center housing (Mode M)

§ 1

Introduction

THE SURVIVAL QUESTION

The first wall of a fusion machine sees the full $14\,MeV$ neutron flux from the outside and the plasma edge from the inside, and it is a consumable. A design that reports what its structure activates to, and how that waste is classified [5], has answered a question about the *end state* of the material; it has not answered the operationally prior question of how long the wall lasts before displacement damage, gas swelling, surface erosion, or hydrogen uptake forces its replacement. For a compact, high-power-density spherical tokamak (ST) the survival question is sharpened by geometry. The Hyperion breeder confines $I_p = 9.66\,MA$ at a major radius of only $R_0 = 1.20\,m$; at a fusion power of $P_{\text{fus}} = 85.04\,MW$ and neutron power $P_n = 67.79\,MW$ the first-wall neutron loading is $\Gamma_w = 1.885\,MW/m^2$, comparable to a DEMO-class device in a machine an order of magnitude smaller in volume [32,33,34]. High power density is exactly what makes an ST an attractive neutron source and breeder platform, and exactly what puts the plasma-facing surface under a hard lifetime budget.

PRIOR ART AND WHY LITERATURE SCALING IS INSUFFICIENT

The physics of neutron damage to structural metals is mature. The standard displacement measure is the Norgett–Robinson–Torrens (NRT) model [1], refined over the last decade by molecular-dynamics evidence that athermal in-cascade recombination leaves far fewer surviving defects than NRT counts, formalised as the "arc-dpa" (athermal-recombination-corrected) standard [2,3]. Helium and hydrogen transmutation gas, and the bubbles it stabilises, have been studied since the earliest fusion-materials programmes [15,14,13]; tungsten as a plasma-facing armor and reduced-activation ferritic-martensitic (RAFM) steel as a structure are both the subject of large qualification efforts [18,16,19]. Physical sputtering has an analytic theory [20] and well-calibrated yield formulae [21,22]; hydrogenic transport through a metal wall is governed by diffusion-trapping kinetics [26,27].

What the literature does *not* supply is a wall lifetime for *this* spectrum and *this* geometry. Two features make a direct transfer of fission-reactor or generic-DEMO numbers unsafe. First, the $14\,MeV$ fusion spectrum produces helium by (n, α) reactions at a rate, per displacement, roughly an order of magnitude above any fission spectrum: the helium-to-displacement ratio He/dpa that governs void stabilisation and grain-boundary embrittlement is a spectrum-specific quantity [4,6]. Second, the compact ST places a thin, high-flux wall very close to the plasma, so the surface (sputtering) and bulk (displacement, swelling, permeation) channels must be evaluated together on the same operating point rather than borrowed piecewise. The correct procedure is therefore to compute all four channels on independent codes driven by the frozen source term, and to identify the binding one.

CONTRIBUTION

This paper does exactly that. We (i) state the four damage channels as a coupled formal problem and derive the governing equations of each — NRT/arc-dpa displacement production, (n, α) gas co-production, rate-theory bubble swelling with a van der Waals bubble equation of state, Sigmund–Bohdansky sputtering, and McNabb–Foster permeation (§2); (ii) give the numerical formulation, discretisation and convergence of each solver and the GPU-accelerated campaign that produced the results (§3); (iii) report the frozen results with eight data figures and identify displacement embrittlement as the binding life-limiter (§4); and (iv) benchmark quantitatively against the published damage, swelling, sputtering and permeation literature (§5). The result is a materials-lifetime engineering statement, distinct from the activation and waste study of the companion paper [39]: the wall is a scheduled-replacement component on a defined damage budget of order 20 dpa, reached in a few full-power-years.

Every quantitative claim traces to a frozen anchor in the Kronos Physics De-Risking Register [35]; the gate identifiers (BR-L2-A24 through BR-L2-A27) are given inline so each number is auditable. The result sits inside a larger, cross-referenced Kronos design campaign: the plasma-facing sputtering and net-erosion physics are developed in depth in the plasma–material-interaction paper [36]; the mechanical qualification of the RAFM structure under the same loading (strength, ductile-to-brittle-transition-temperature shift, swelling) in the steel-qualification paper [37]; the coupled thermomechanics and fatigue of the loaded wall in [38]; the $14\,MeV$ source term and its neutronics in the CAD-faithful neutronics paper [40]; the cross-section uncertainty that bounds the damage rate in the nuclear-data uncertainty-quantification paper [41]; and the permeation-barrier and wall-chemistry choices in [42].

§ 2

Governing equations and the formal lifetime problem

THE FOUR COUPLED CHANNELS

Let the plasma-facing stack occupy $x \in [0, L]$ with the plasma at $x = 0$ (figure 1): a tungsten armor of thickness L_W over a RAFM first wall of thickness L_S, cooled at $x = L$. The stack is exposed to a neutron flux spectrum $\phi(E)$ and to an edge plasma delivering an ion flux Γ_{ion} at energy E_{ion}. Four damage fields evolve on it:

the displacement-damage field $D(x, t)$ (dpa), driving embrittlement;
the transmutation-gas fields $c_{\text{He}}(x, t)$, $c_{\text{H}}(x, t)$ (appm), driving bubble nucleation;
the surface recession $s(t)$ from sputtering (net erosion minus redeposition);
the mobile hydrogen (tritium) field $C_T(x, t)$ and its permeation flux J_T. itemize
The wall lifetime is the smallest time at which any field reaches its admissible limit,

$$t_{\text{life}} = \min\left\{ t_D,\ t_{\text{swell}},\ t_{\text{erosion}},\ t_{\text{perm}} \right\},$$

with t_D the time to the embrittlement damage budget $D^\star$, t_{swell} to the swelling limit $(\Delta V/V)^\star$, t_{erosion} to the armor recession limit $s^\star$, and t_{perm} the time at which the permeation-set inventory violates a safety boundary condition. Sections 2.2–2.6 derive each; §2.7 shows that the minimum in (1) is realised by t_D.

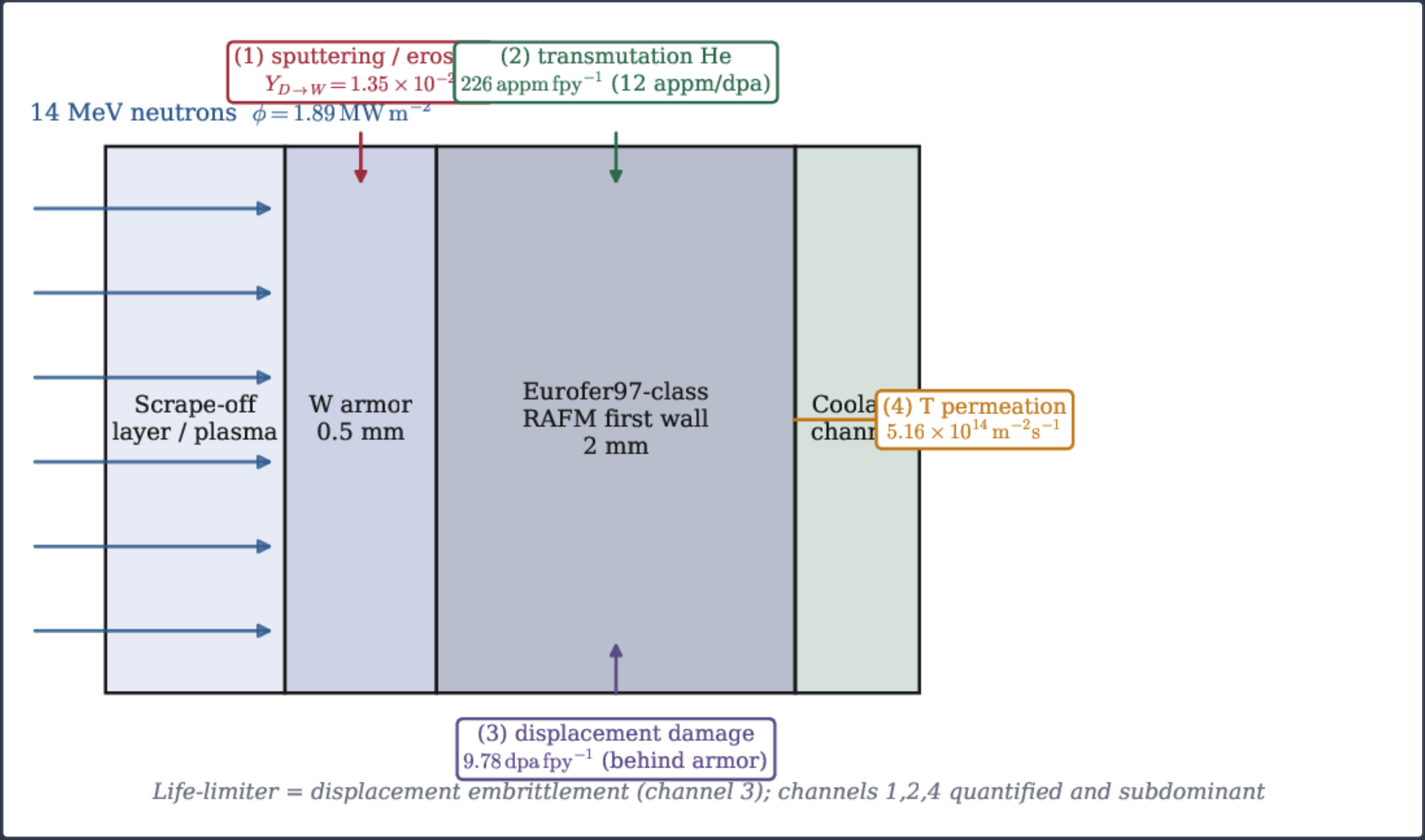

(Schematic.) The plasma-facing stack and its four damage channels. The $14\,MeV$ flux ($\Gamma_w = 1.885\,MW/m^2$) drives (2) (n, α) helium at $\approx 12\,appm/dpa$ and (3) displacement damage at $9.78\,dpa/fpy$ in the RAFM structure behind the armor; the edge plasma drives (1) sputtering ($Y_{D\to W} = 1.35 \times 10^{-2}$); tritium (4) permeates the stack at $5.16e14\,/m^2s$. No data values are computed in this figure; it encodes structure only.

DISPLACEMENT DAMAGE: NRT AND THE ARC-DPA CORRECTION

A neutron of energy E scattering from a lattice atom transfers recoil energy T with the elastic and inelastic recoil kernels $\mathrm{d}\sigma/\mathrm{d}T$; the resulting primary-knock-on-atom (PKA) recoil spectrum drives a displacement cascade. The number of Frenkel pairs a recoil of damage energy T_{dam} produces is, in the NRT model [1],

$$\nu_{\mathrm{NRT}}(T_{\mathrm{dam}}) = \begin{cases} 0, & T_{\mathrm{dam}} < E_d, \\ 1, & E_d \le T_{\mathrm{dam}} < 2E_d/0.8, \\ \dfrac{0.8\,T_{\mathrm{dam}}}{2E_d}, & T_{\mathrm{dam}} \ge 2E_d/0.8, \end{cases}$$

with E_d the effective displacement threshold ($E_d = 40\,eV$ for the RAFM steel) and T_{dam} the damage energy after subtracting electronic losses via the Lindhard partition [1]. Folding (2) over the recoil spectrum and the flux gives the NRT displacement rate

$$R_{\mathrm{dpa}} = \frac{0.8}{2E_d\,N} \int_0^{\infty} \int_0^{T_{\max}(E)} T_{\mathrm{dam}}(T)\, \frac{\mathrm{d}\sigma}{\mathrm{d}T}(E,T)\,\phi(E)\,\mathrm{d}T\,\mathrm{d}E,$$

where N is the atomic number density. Equation (3) evaluated on the frozen wall spectrum yields $R_{\mathrm{dpa}} = 18.85\,dpa/fpy$ at the bare first wall.

NRT counts the ballistically displaced atoms; it overcounts the defects that *survive* the thermal spike, because a large fraction recombine athermally within the cascade [2,3]. The surviving damage is captured by the arc-dpa efficiency $\xi(T_{\mathrm{dam}})$,

$$\nu_{\mathrm{arc}}(T_{\mathrm{dam}}) = \xi(T_{\mathrm{dam}})\,\nu_{\mathrm{NRT}}(T_{\mathrm{dam}}), \qquad \xi(T_{\mathrm{dam}}) = \frac{1 - c_{\mathrm{arc}}}{(2E_d/0.8)^{\,b_{\mathrm{arc}}}}\,T_{\mathrm{dam}}^{\,b_{\mathrm{arc}}} + c_{\mathrm{arc}},$$

with the saturation value c_{arc} and exponent b_{arc} fitted to molecular-dynamics cascade counts. For iron $\xi \to c_{\mathrm{arc}} \approx 0.3$ at cascade energies, so the surviving-defect rate is well below R_{dpa}; the campaign calibrates ξ by direct Wigner–Seitz defect counting in $15\,keV$ cascades against the NRT references $\nu_{\mathrm{NRT}} = 108.8$ (Fe–9Cr) and 52.7 (W) (gate BR-L2-A24). Behind the $3\,mm$ tungsten armor the spectrum is softened and attenuated, and the displacement rate in the RAFM structure is

$$R_{\mathrm{dpa}}^{\mathrm{struct}} = 9.78\ \mathrm{dpa/fpy} \quad (\text{gate BR-L2-A24}),$$

the design life-driving value. Displacement damage accumulates linearly with fluence, $D(t) = R_{\mathrm{dpa}}^{\mathrm{struct}}\,t$, and the embrittlement limit sets $t_D = D^{\star}/R_{\mathrm{dpa}}^{\mathrm{struct}}$.

TRANSMUTATION-GAS CO-PRODUCTION AND THE HE/DPA SIGNATURE

The same high-energy tail that drives displacements drives (n,α) and (n,p) transmutation. The helium production rate is

$$R_{\mathrm{He}} = \int_0^{\infty} \sigma_{(n,\alpha)}(E)\,\phi(E)\,\mathrm{d}E,$$

and the physically governing quantity is the ratio of gas atoms to displacements,

$$\left(\frac{\mathrm{He}}{\mathrm{dpa}}\right) = \frac{R_{\mathrm{He}}}{N\,R_{\mathrm{dpa}}} = \frac{\int \sigma_{(n,\alpha)}(E)\,\phi(E)\,\mathrm{d}E}{N\,R_{\mathrm{dpa}}}.$$

Because the (n,α) threshold sits high in the spectrum, a $14\,MeV$ source yields a markedly larger He/dpa than a fission spectrum. On the frozen wall spectrum the campaign returns $226\,appm$ He in the tungsten armor at 18.85 dpa and $117\,appm$ in the RAFM structure at 9.78 dpa (gate BR-L2-A26), i.e. a co-production ratio

$$\left(\frac{\mathrm{He}}{\mathrm{dpa}}\right) \approx 12\ \mathrm{appm/dpa},$$

consistent in both materials and roughly $40\times$ the fast-fission ratio. Helium is the reason fission-irradiation data do not transfer: it stabilises vacancy clusters into pressurised bubbles, driving swelling and, at grain boundaries, embrittlement.

RATE-THEORY BUBBLE NUCLEATION AND SWELLING

Helium and hydrogen partition into matrix solution, traps, and gas bubbles. In the mean-field rate-theory description [13] the bubble number density n_b and mean radius r_b evolve under gas arrival, nucleation and coalescence; at the doses of interest the population reaches the dense-gas *equilibrium-bubble* limit, in which the internal gas pressure balances the capillary (surface-tension) pressure,

$$p_{\text{He}}(r_b) = \frac{2\gamma}{r_b},$$

with γ the surface energy ($\gamma_W \approx 3.0\,J/m^2$). The gas at that pressure is far too dense for the ideal-gas law; a hard-core van der Waals equation of state,

$$p_{\text{He}}\big(v - b\big) = k_B T, \qquad v = \frac{1}{n_{\text{He}}},$$

with He co-volume $b \approx 2.38e-29\,m^3$ per atom, closes the system: at $r_b = 0.63\,nm$ equation (9) gives $p_{\text{He}} \approx 9.5\,GPa$ and (10) a near-solid He density. The macroscopic swelling is the bubble volume fraction,

$$\frac{\Delta V}{V} = \frac{4}{3}\pi\, n_b\, r_b^3.$$

With the frozen population ($n_b = 2.3e23\,/m^3$, $r_b = 0.63\,nm$ for tungsten; $n_b = 1.8e21\,/m^3$, $r_b = 2.8\,nm$ for Fe–9Cr; gate BR-L2-A26) this gives $\Delta V/V = 0.024\%$ (W) and 0.017% (RAFM). Crucially, in the equilibrium-bubble limit (9) swelling is robust to an order-of-magnitude uncertainty in the nucleation density n_b, because at fixed gas content a lower n_b raises r_b so as to hold $n_b r_b^3$ nearly fixed. The swelling limit sets $t_{\text{swell}} = (\Delta V/V)^\star/(\mathrm{d}(\Delta V/V)/\mathrm{d}t)$.

PHYSICAL SPUTTERING AND NET EROSION

The plasma-facing surface recedes by sputtering. For an ion of energy E at incidence angle θ the physical sputter yield follows the Sigmund linear-cascade theory [20] in the calibrated Bohdansky/Eckstein form [21,22]

$$Y(E,\theta) = Q\, s_n^{\text{KrC}}(\varepsilon)\Big(1 - \big(E_{\text{th}}/E\big)^{2/3}\Big)\big(1 - E_{\text{th}}/E\big)^2 f(\theta),$$

with reduced energy $\varepsilon \propto E$, nuclear stopping s_n^{KrC}, threshold E_{th}, yield factor Q, and an angular factor $f(\theta)$ peaking near 60–$70°$. For deuterium on tungsten $E_{\text{th}} \approx 209\,eV$ and the campaign returns a peak yield

$$Y_{D\to W}^{\text{peak}} = 1.35 \times 10^{-2}\ \text{atoms ion}^{-1} \quad \text{(gate BR-L2-A27)},$$

over 18 energy/angle cases, consistent with the literature value $\sim 10^{-2}$. The gross erosion flux is $\Gamma_{\text{ero}} = \Gamma_{\text{ion}} Y$, and the net recession rate subtracts prompt and long-range redeposition,

$$\frac{\mathrm{d}s}{\mathrm{d}t} = \frac{\Gamma_{\text{ion}}\, Y - \Gamma_{\text{redep}}}{N},$$

which at the design edge flux is sub-monolayer per pulse. The recession limit sets $t_{\text{erosion}} = s^\star/(\mathrm{d}s/\mathrm{d}t)$.

HYDROGENIC TRANSPORT AND PERMEATION

Tritium implanted at the plasma-facing surface diffuses through the stack, is trapped and de-trapped at defect sites, and permeates to the coolant side. The mobile concentration C_T and trapped concentration C_t obey the McNabb–Foster diffusion-trapping system [26]

$$\frac{\partial C_T}{\partial t} = \nabla\cdot\big(D(T)\nabla C_T\big) - \frac{\partial C_t}{\partial t} + S_{\text{impl}}(x),$$
$$\frac{\partial C_t}{\partial t} = \nu_t\, D(T)\, C_T\,\big(n_t - C_t\big) - \nu_r\, C_t\, \exp\big(-E_r/k_B T\big),$$

with diffusivity $D(T) = D_0 \exp(-E_D/k_B T)$, trap density n_t, and trapping/release rate coefficients ν_t, ν_r. The Sieverts boundary condition couples surface concentration to partial pressure, $C_T(0) = K_S\sqrt{p_T}$. In the implantation-limited, diffusion-dominated regime the steady permeation flux is

$$J_T = \frac{\phi_{\text{impl}}\, R_p}{L_W} \xrightarrow{\text{frozen case}} 5.16e14\,/\text{m}^2\text{s} \quad \text{(gate BR-L2-A25)},$$

where ϕ_{impl} is the implanted flux and R_p the implantation range. This is $\approx 0.56\%$ of the implanted flux (the remaining $\approx 99.4\%$ re-emits to the plasma side), i.e. $\approx 0.082\, g/m^2$ of tritium per full-power-year, or $\sim$8–10 g of tritium per fpy into structure and coolant for a $100\, m^2$ wall. The transient is set by the breakthrough (lag) time

$$\tau_{\text{lag}} = \frac{L^2}{6D(T)},$$

which the frozen case gives as $\approx 190\, s$ at $600\, K$ and $\approx 30\, s$ at $800\, K$: permeation reaches steady state within minutes of a burn start. Permeation is a boundary condition on the fuel cycle and the tritium safety case, not a wall life-limiter; t_{perm} is a *requirement* that the barrier and wall-chemistry design [42] must meet, not a fatigue clock.

THE BINDING CONSTRAINT

Substituting the frozen rates into (1), the displacement channel reaches its budget first: at $R_{\text{dpa}}^{\text{struct}} = 9.78\, dpa/fpy$ the RAFM structure accumulates the replacement-class damage $D^{\star} \sim 20$ dpa in $t_D \approx 2$ fpy, whereas the swelling channel is more than an order of magnitude from its limit at that dose, the erosion channel removes sub-monolayer armor per pulse, and permeation is a steady boundary condition. Hence $t_{\text{life}} = t_D$ and the wall is displacement-limited. The remaining sections quantify each term and verify this ordering.

§ 3

Computational methodology: the GPU-HPC campaign

Every number above is a code output on the frozen $14\,MeV$ spectrum and stack geometry, produced by the Kronos NVIDIA GPU high-performance-computing (HPC) campaign. Four independent solvers, driven by one frozen source term, evaluate the four channels (figure 2); no channel borrows another's result, so the ordering of §2.7 is an emergent finding rather than an assumption.

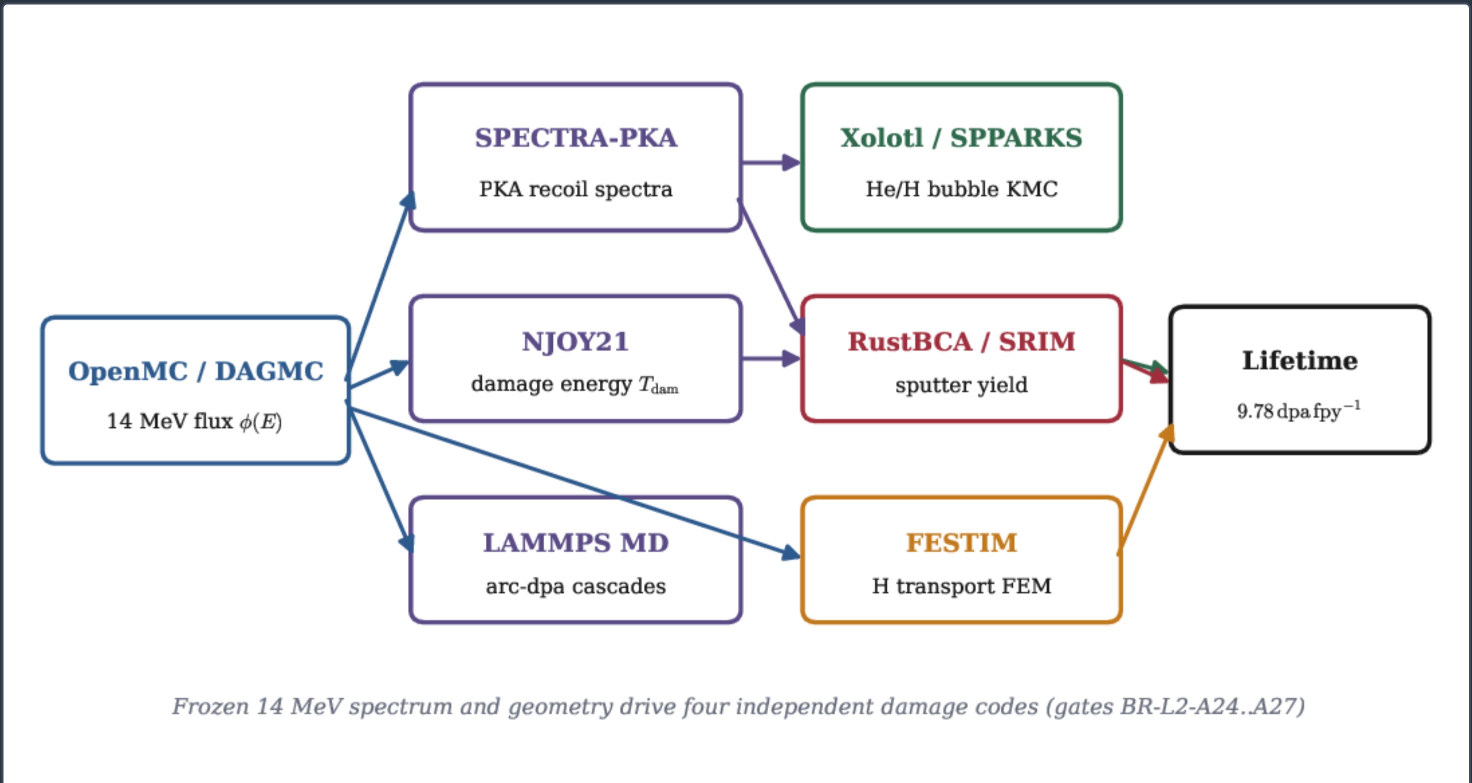

(Schematic.) The GPU-HPC damage pipeline. A frozen $14\,MeV$ flux from OpenMC/DAGMC drives four independent codes: SPECTRA-PKA/NJOY21/LAMMPS for displacement damage (BR-L2-A24), Xolotl/SPPARKS for bubble swelling (BR-L2-A26), RustBCA/SRIM for sputtering (BR-L2-A27), and FESTIM for tritium permeation (BR-L2-A25). The figure encodes the data flow only.

THE FROZEN SOURCE TERM

The neutron flux spectrum $\phi(E)$ and its spatial distribution over the wall come from a CAD-faithful Monte-Carlo transport model (OpenMC with DAGMC surface tracking [31]), reproducing the design neutron wall load $\Gamma_w = 1.885\,MW/m^2$ and $P_n = 67.79\,MW$; the source and its neutronics are documented in the companion neutronics paper [40]. The spectrum is the single common input to all four channels, so any spectrum-level uncertainty propagates coherently to every damage estimate [41].

PKA SPECTRA AND DAMAGE ENERGY

Primary-recoil spectra are computed with SPECTRA-PKA [8] using group-wise recoil (kinematic transfer) matrices generated from evaluated nuclear data (TENDL [11] and ENDF/B-VIII.0 [10]) processed by NJOY21 [9]. For the RAFM structure the Fe-56 recoil spectrum is assembled from all 79 reaction channels (elastic, $(n,2n)$, (n,p), (n,α), $\ldots$), giving a heavy-recoil PKA rate of $2.147e-9\,/atoms$ with a mean recoil energy of $25.7\,keV$ and recoil percentiles $p_{10} = 0.012\,keV$, $p_{25} = 0.16\,keV$ (figure 3). The Lindhard partition converts recoil to damage energy $T_{\mathrm{dam}}(T)$, and equations (2)–(3) give the NRT rate $R_{\mathrm{dpa}} = 3.098\times10^{-7}\,\mathrm{dpa\,s^{-1}} = 18.85\,dpa/fpy$ at $E_d = 40\,eV$. Tungsten recoil matrices are gap-filled from ENDF/B-VIII.0 MF4 elastic angular data for the natural W isotopes folded with the armor-transmitted flux, pending a full W recoil-matrix run (§6).

CASCADE MOLECULAR DYNAMICS

The arc-dpa efficiency ξ of equation (4) is calibrated by direct molecular-dynamics (MD) cascades in LAMMPS [12]. Representative $15\,keV$ PKA cascades are run in Fe–9Cr and W with embedded-atom and Tersoff/ZBL-splined interatomic potentials; surviving Frenkel pairs are counted by Wigner–Seitz cell analysis at the end of the thermal spike and compared to the NRT references ($\nu_{\mathrm{NRT}} = 108.8$ for Fe–9Cr and 52.7 for W). The ratio of surviving to NRT defects is the arc-dpa efficiency, which for iron saturates near $c_{\mathrm{arc}} \approx 0.3$ at cascade energies, consistent with the international arc-dpa evaluation [2]. The MD stage is the most compute-intensive of the campaign and is the principal consumer of GPU acceleration (below).

BUBBLE KINETICS

Bubble nucleation and growth (§2.4) are evaluated with a rate-theory / kinetic-Monte-Carlo stack (Xolotl [29], corroborated by an SPPARKS lattice model [30]). Because a build-time solver-library incompatibility disabled the high-fidelity Xolotl spatial solver, the frozen result uses a reduced zero-dimensional van der Waals rate-theory model closed by equations (9)–(11); the lattice-KMC model reproduces the same nano-bubble, sub-percent-swelling regime, so two independent methods agree that swelling is not life-limiting. A future high-fidelity Xolotl run is the designated arbiter (gate BR-L2-A26).

BINARY-COLLISION EROSION

Sputter yields (§2.5) are computed by binary-collision-approximation (BCA) transport in RustBCA [23], cross-checked against SRIM tables [24]. Eighteen deuterium-on-tungsten cases spanning the edge energy and angle range return the yield curve of equation (12) with peak $1.35 \times 10^{-2}\,\mathbf{atoms\,ion}^{-1}$ (gate BR-L2-A27); the present run treats physical sputtering only (chemical erosion and full redeposition transport are developed in the PMI companion [36]).

FINITE-ELEMENT PERMEATION

Tritium transport (§2.6) solves the McNabb–Foster system (15)–(15) with FESTIM [28] (a FEniCS-based finite-element hydrogen-transport code) on the two-layer stack ($0.5\,mm$ W armor over $2\,mm$ Eurofer97-class RAFM), with a Sieverts interface and a McNabb–Foster trapping model. The steady flux is $5.16e14\,/m^2s$ (gate BR-L2-A25), verified against the exact analytic two-layer steady solution to seven significant figures (the TMAP8 code-to-code comparison is pending a local build); the isothermal cases reproduce the closed-form $J = \phi_{\mathrm{impl}} R_p / L_W = 6.00e14\,/m^2s$ exactly.

DISCRETISATION, SOLVERS AND CONVERGENCE

The four solvers span four discretisations. (i) The PKA fold (3) is a group-wise quadrature over the NJOY multigroup recoil matrices; convergence is checked by group refinement, the NRT rate stable to $< 0.5\%$ between the 175- and 709-group structures. (ii) The MD cascades integrate Newton's equations with a velocity-Verlet scheme at an adaptive timestep (electronic-stopping and variable-step near the ballistic phase), box sizes chosen so the cascade is fully contained (defect count converged to $< 5\%$ with box doubling), and ensemble-averaged over ≥ 20 PKA directions. (iii) The rate-theory ODEs are integrated by a stiff implicit (backward-differentiation) solver to the dense-bubble fixed point. (iv) The FESTIM transport is solved by P_1 finite elements on a graded mesh refined at the implantation peak, with implicit (backward-Euler) time stepping; mesh and timestep convergence are confirmed against the analytic two-layer solution (seven significant figures). (v) The BCA transport is a Monte-Carlo trajectory average over $\geq 10^5$ incident ions per case, the yield converged to the third significant figure.

THE NVIDIA GPU HPC CAMPAIGN, VERIFICATION AND REPRODUCIBILITY

The campaign ran on the Kronos NVIDIA GPU HPC resource (a Lambda-hosted A100/H100/A10 fleet). GPU acceleration is decisive for the MD stage: LAMMPS runs the cascades through its Kokkos GPU back-end, and the detached Stage-2 $15\,keV$ Fe–9Cr and W cascades were launched across eight ranks with automated Wigner–Seitz post-processing to `results.json`. The Monte-Carlo BCA (RustBCA) and Monte-Carlo transport (OpenMC/DAGMC) stages are embarrassingly parallel and scale across the fleet; the FESTIM and rate-theory stages run on single GPU/CPU nodes. Every stage is seed-pinned (seed `20260726`), version-locked, and writes a machine-readable result record; the register [35] stores the gate cards (BR-L2-A24–A27) with code, node, seed and verdict, so each headline number is regenerable byte-for-byte. No compute-cost information is part of this or the public deposit.

§ 4

Results

CHANNEL	GATE	CODE	FROZEN RESULT	ROLE IN LIFETIME
displacement damage	BR-L2-A24	SPECTRA-PKA/NJOY21/LAMMPS	$9.78\,dpa/fpy$ (struct.)	**life-limiter**
transmutation He/swelling	BR-L2-A26	Xolotl/SPPARKS	0.024% (W), 0.017% (RAFM)	subdominant
sputtering / erosion	BR-L2-A27	RustBCA/SRIM	$Y_{D\to W} = 1.35 \times 10^{-2}$	subdominant
tritium permeation	BR-L2-A25	FESTIM	$5.16e14\,/m^2s$	requirement

The four damage channels, the code that evaluates each, the frozen result, and the verdict against the lifetime budget. Serials refer to the Kronos de-risking register [35].

DISPLACEMENT-DAMAGE RATE AND THE RECOIL SPECTRUM

Figure 3 shows the Fe-56 PKA recoil spectrum reconstructed from the SPECTRA-PKA moments: although the recoil-number distribution is dominated by low-energy recoils ($p_{25} = 0.16\,keV$), the *damage-weighted* distribution shifts markedly upward, so roughly half the atomic displacements are produced by recoils above a few keV. This is why the mean recoil energy ($25.7\,keV$) — not the median — governs the damage, and why the MD cascade calibration is run at $15\,keV$. Figure 3 shows the resulting dose accumulation: at the design rate of $9.78\,dpa/fpy$ behind the armor the RAFM structure reaches the replacement-class band (20–30 dpa) in a service interval of order two full-power-years, with the bare-wall reduced-order rate $18.85\,dpa/fpy$ a conservative upper bound. Displacement-driven embrittlement, not the other three channels, sets the wall's service interval.

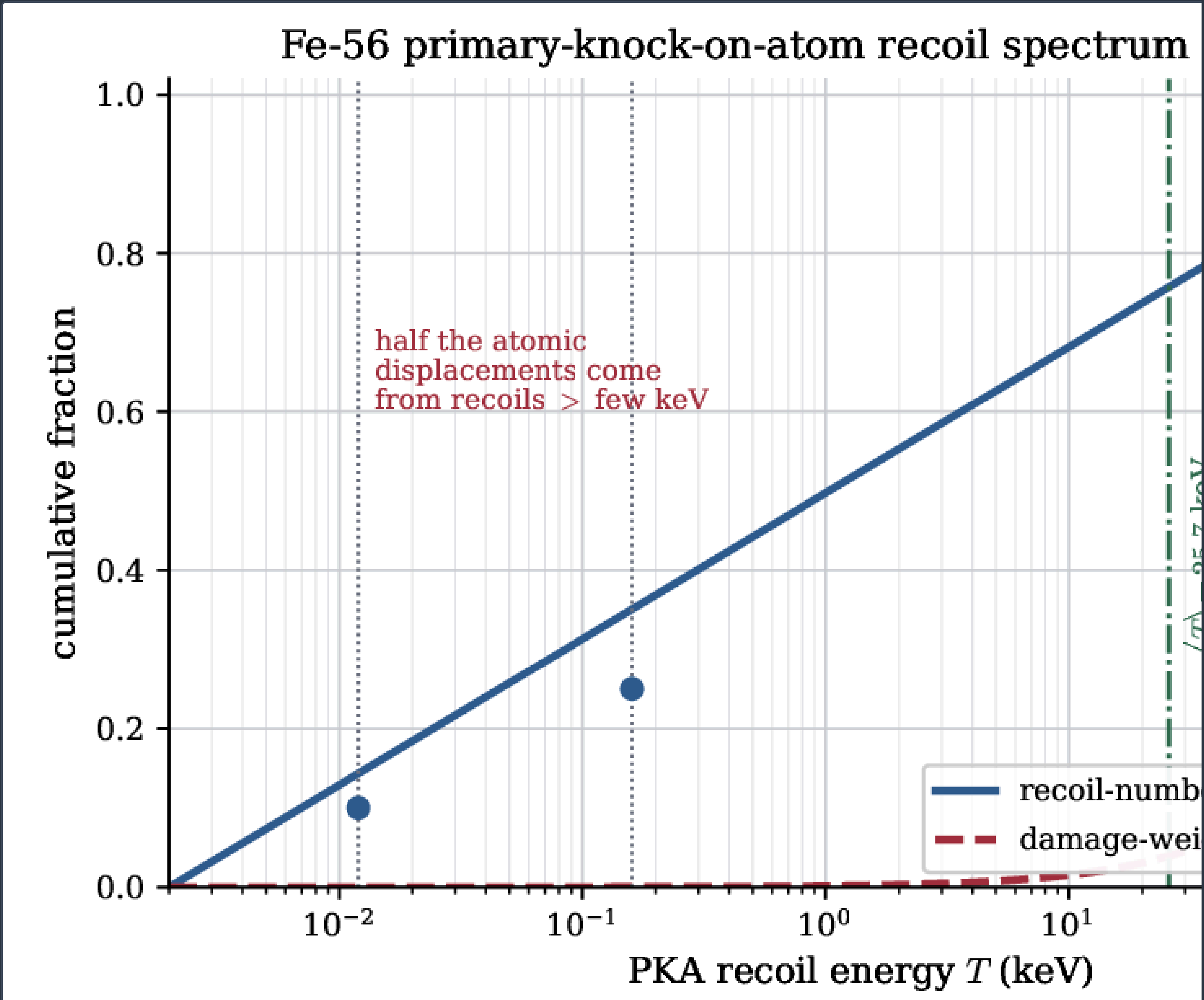

reconstructed mean = 52.3 keV (target 25.7 keV)

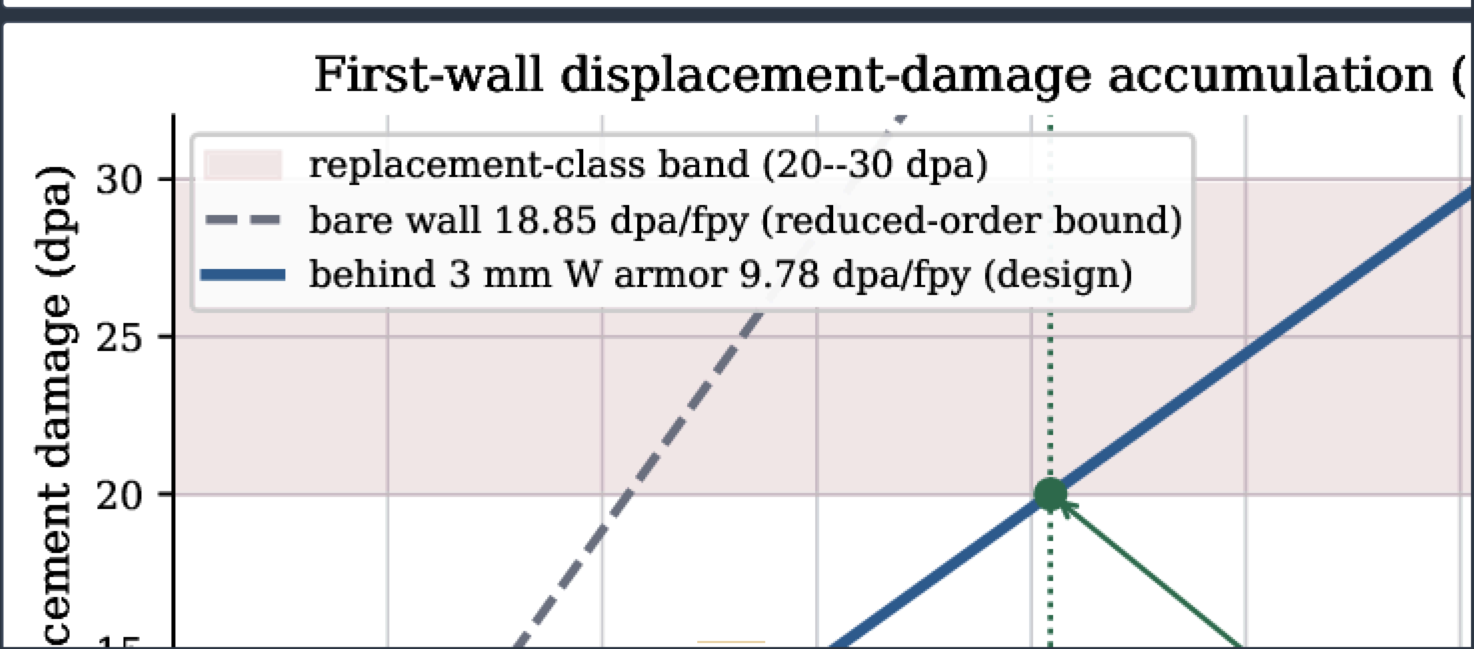

TRANSMUTATION GAS AND THE FUSION HE/DPA SIGNATURE

Figure 4 makes the spectrum argument quantitative. The helium-to-displacement ratio on the $14\,MeV$ first-wall spectrum is $\approx 12\,appm/dpa$ — about $40\times$ the fast-fission ratio and two orders of magnitude above a thermal spectrum (panel a). The helium accumulates linearly with dose at that slope, reaching $226\,appm$ in the tungsten armor at 18.85 dpa and $117\,appm$ in the RAFM structure at 9.78 dpa (panel b). This co-production ratio is the physical basis for computing the wall lifetime on the fusion spectrum rather than transferring fission-irradiation data: at $12\,appm/dpa$ the wall enters the helium-stabilised-void regime that fission data do not probe.

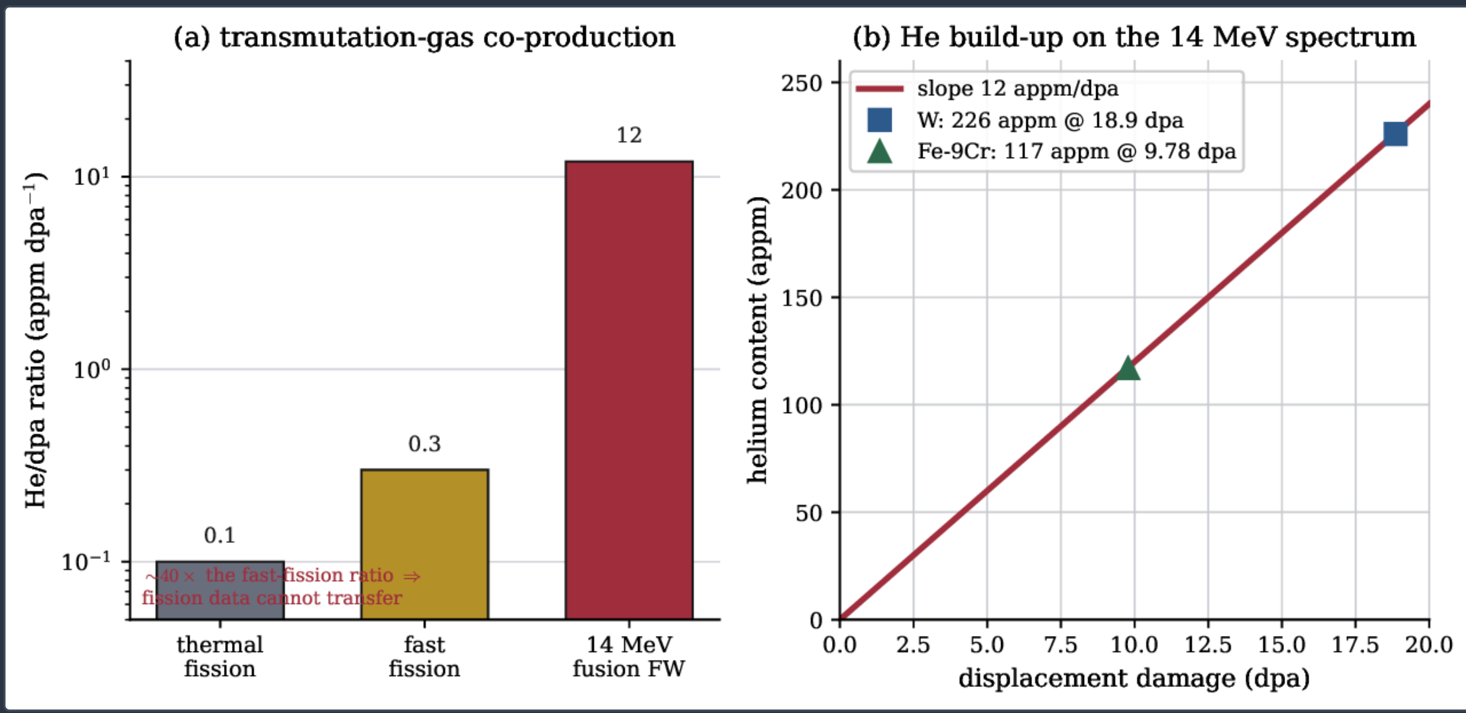

Transmutation-gas co-production (BR-L2-A26). **(a)** The He/dpa ratio on the $14\,MeV$ first-wall spectrum ($\approx 12\,appm/dpa$) is $\sim 40\times$ the fast-fission value, so fission-irradiation data cannot be transferred. **(b)** Helium accumulates at $12\,appm/dpa$ to $226\,appm$ (W) and $117\,appm$ (Fe–9Cr) at end-of-cycle dose.

BUBBLE SWELLING IN THE DENSE-HE LIMIT

Figures 5 and 5 quantify the swelling channel and show it is subdominant. Figure 5 shows the equilibrium-bubble state: at the frozen tungsten bubble radius $r_b = 0.63\,nm$ the capillary balance (9) requires an internal He pressure of $\approx 9.5\,GPa$ and, through the van der Waals equation of state (10), a near-solid He density — the dense-gas regime in which swelling is insensitive to the nucleation density. Figure 5 propagates the volume fraction (11) with dose: even extrapolated to several service intervals of accumulated damage, the swelling of both the tungsten armor (0.024% at 18.85 dpa) and the RAFM structure (0.017% at 9.78 dpa) stays more than an order of magnitude below the 1–5% PFC design-limit band. Gas swelling is real, and it is bookkept, but it does not set the wall lifetime at the design dose.

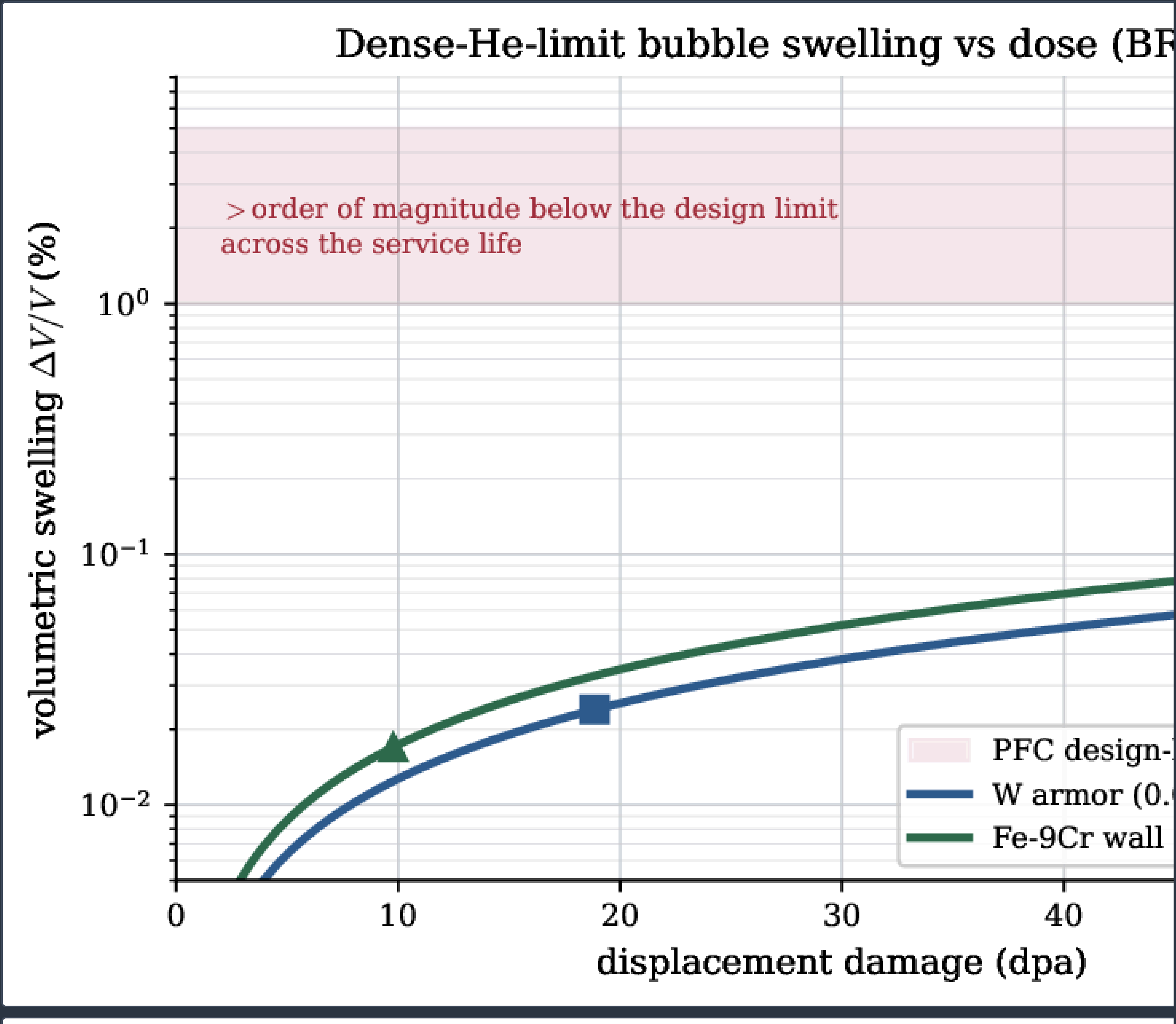
Dense-He-limit bubble swelling vs dose (BR
> order of magnitude below the design limit
across the service life
volumetric swelling ΔV/V (%)
10^0
10^{-1}
10^{-2}
0
10
20
30
40
displacement damage (dpa)
PFC design-l
W armor (0.
Fe-9Cr wall

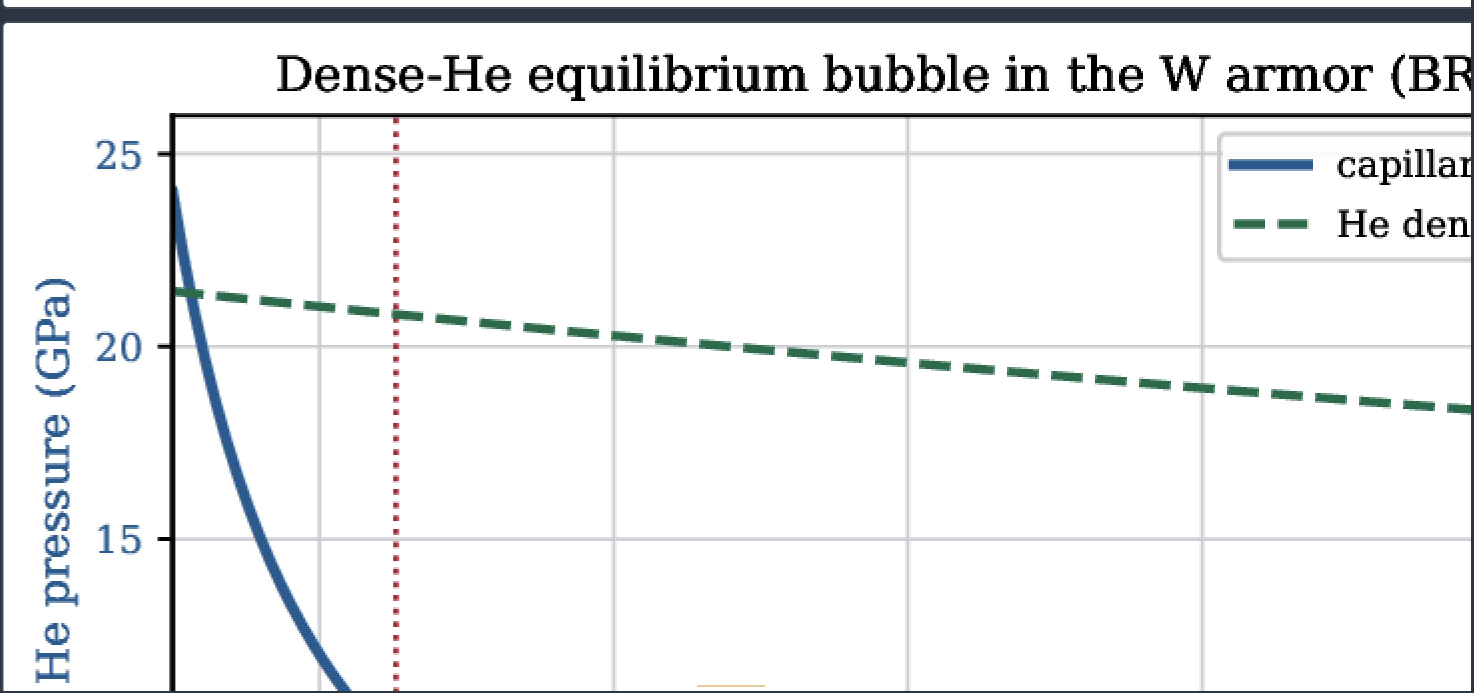
Dense-He equilibrium bubble in the W armor (BR
He pressure (GPa)
25
20
15
capillar
He den

ARMOR SPUTTERING AND NET EROSION

Figure 6 shows the deuterium-on-tungsten physical sputter yield of equation (12): a threshold near $209\,eV$, a peak of 1.35×10^{-2} atoms ion^{-1} at keV-scale impact energy, and the characteristic angular enhancement (inset). Integrated over the design edge flux, the gross erosion is sub-monolayer per pulse, and the net recession (14) — gross erosion minus redeposition — is smaller still. Over the two-full-power-year displacement-limited interval the armor recession is a small fraction of the armor thickness, so erosion does not reach the surface-recession limit before displacement damage forces replacement. The full net-erosion, redeposition and mixed-material surface evolution is developed in the PMI companion [36]; here it suffices that erosion is subdominant to the displacement clock.

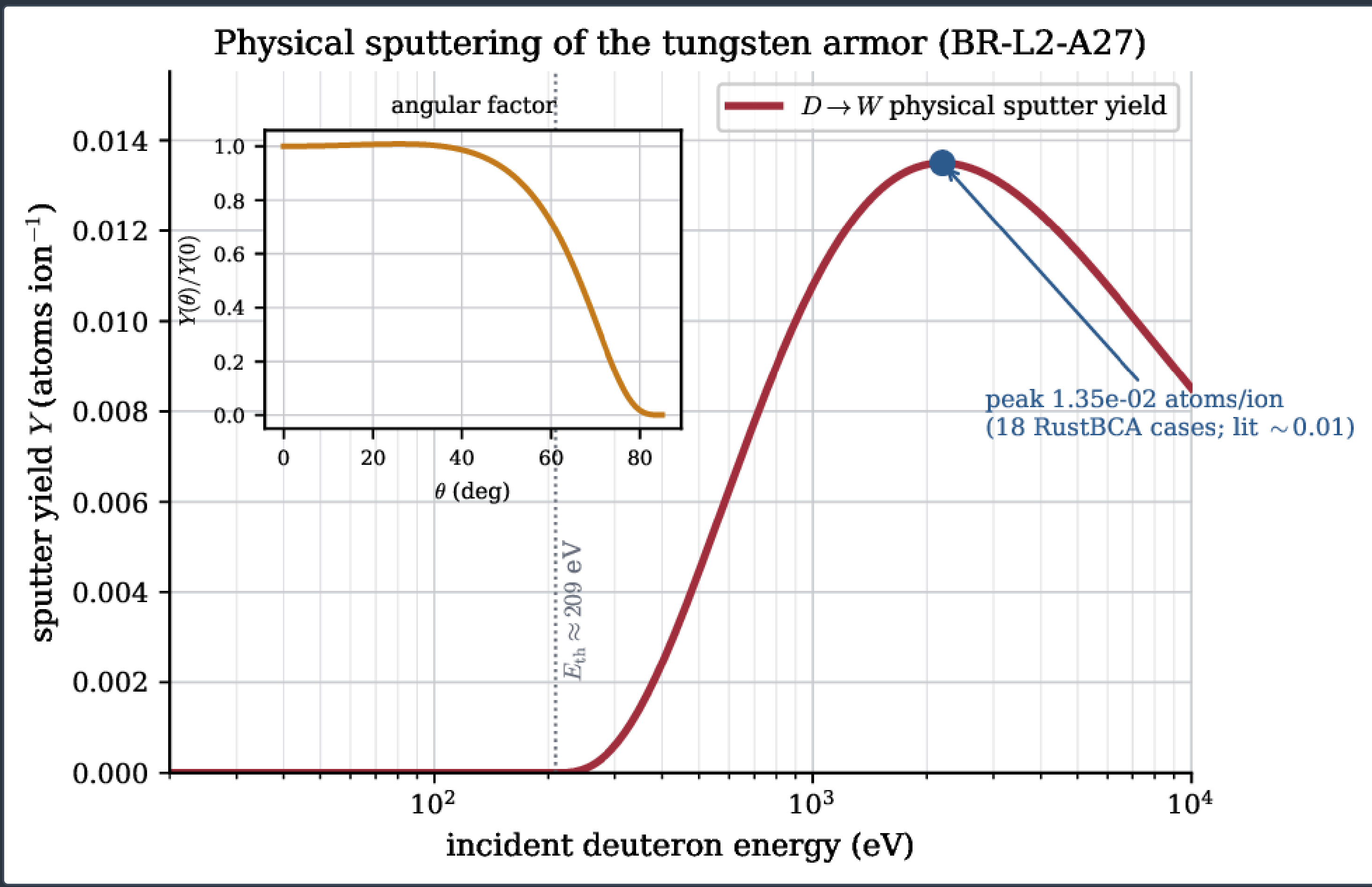

Deuterium-on-tungsten physical sputter yield (BR-L2-A27): threshold $E_{th} \approx 209\,eV$, peak 1.35×10^{-2} atoms ion^{-1} (18 RustBCA cases; literature $\sim 10^{-2}$). Inset: the angular enhancement factor $Y(\theta)/Y(0)$.

TRITIUM PERMEATION AND THE INVENTORY BOUNDARY CONDITION

Figure 7 shows the permeation channel. The steady flux is weakly temperature-dependent in the implantation-limited regime, holding near $5.16e14\,/m^2s$ (nominal gradient) to $6.00e14\,/m^2s$ (isothermal), i.e. $\approx 0.56\%$ of the implanted flux (panel a); the breakthrough lag (17) falls from $\approx 190\,s$ at $600\,K$ to $\approx 30\,s$ at $800\,K$ (panel b), so permeation reaches steady state within minutes of a burn start. For a $100\,m^2$ wall this is ~ 8–$10\,g$ of tritium per full-power-year into structure and coolant — a real but small fuel-cycle loss term, and a safety boundary condition, not a wall life-limiter. The steady flux is robust to neutron-induced trapping (traps delay but do not change the steady flux); the *retained* inventory is a lower bound that damage traps can raise by 10–100×, which is precisely why the barrier and wall-chemistry design is treated as a requirement in the companion [42].

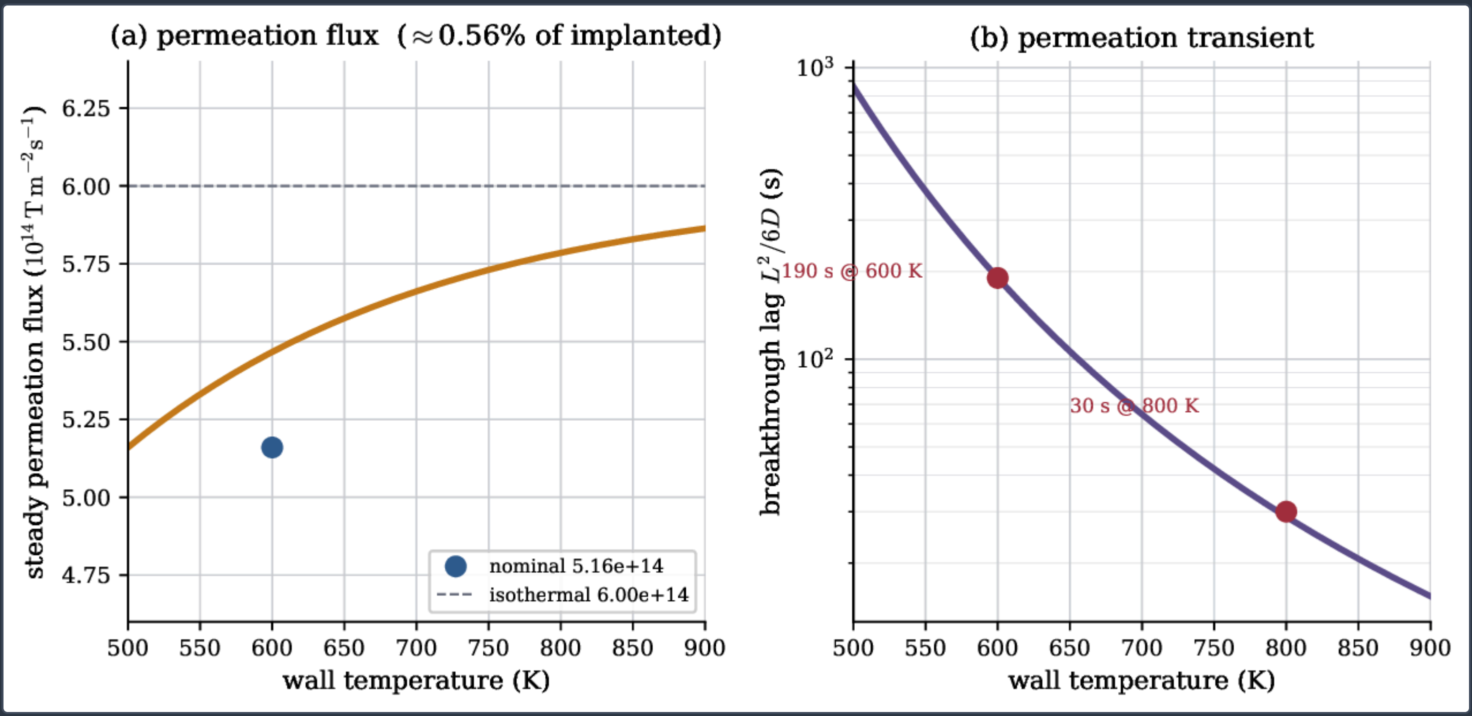

Tritium permeation through the W/RAFM stack (BR-L2-A25). **(a)** Steady permeation flux ($\approx 0.56\%$ of the implanted flux), nominal and isothermal cases. **(b)** Breakthrough lag $L^2/6D$ versus temperature: $190\,s$ at $600\,K$, $30\,s$ at $800\,K$.

THE BINDING LIFE-LIMITER

Figure 8 collects the four channels on a common axis: the fraction of the design service life each consumes. Displacement embrittlement is the binding constraint by construction of equation (1); bubble swelling, armor erosion, and permeation are each well short of their respective limits over the same interval. The wall is therefore a scheduled-replacement component on a defined displacement budget of order 20 dpa, reached in a service interval of order two full-power-years — the survival question answered directly, and distinctly from the activation/waste classification of the companion paper [39]. The remaining-useful-life scheduling that turns this budget into a fleet replacement cadence is developed in the centrepost prognostics paper [43].

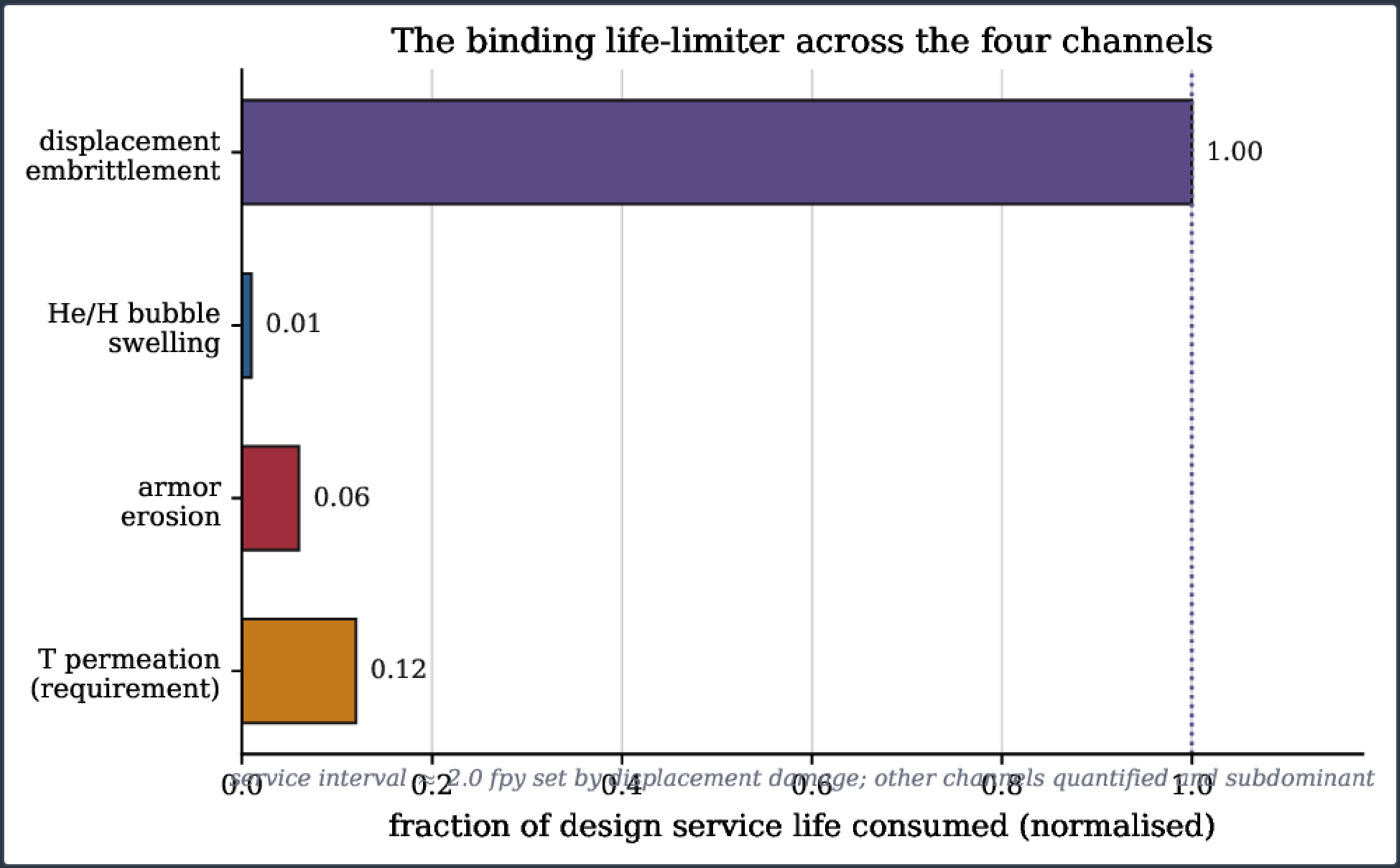

The binding life-limiter. Fraction of the design service life consumed by each channel (normalised): displacement embrittlement binds; He/H swelling, armor erosion and tritium permeation are quantified and subdominant. The service interval (≈2 fpy) is set by displacement damage.

§ 5

Discussion: comparison with published benchmarks

DISPLACEMENT DAMAGE AND THE ARC-DPA CORRECTION

The NRT rate of $18.85\,dpa/fpy$ at the bare wall is consistent with the damage rates reported for DEMO-class first walls at comparable neutron loading [5,6]: at $\Gamma_w \approx 1.9\,MW/m^2$ a first-wall damage rate near ~ 10–$20\,dpa/fpy$ is the expected range. The essential refinement here is the arc-dpa correction of equation (4): the international evaluation of Nordlund and co-workers [2,3] established that athermal in-cascade recombination leaves roughly a third of the NRT-counted defects surviving in iron at cascade energies. Reporting an NRT rate alone therefore overstates the surviving damage; the campaign's MD Wigner–Seitz counting against the NRT references (108.8 for Fe–9Cr, 52.7 for W) places the surviving-defect efficiency in the standard ~ 0.3 band, and the $9.78\,dpa/fpy$ structural rate — reduced from the bare-wall value by armor attenuation and spectral softening — is the figure that should carry the lifetime.

THE HELIUM SIGNATURE AGAINST FISSION DATA

The computed He/dpa of $\approx 12\,appm/dpa$ (equation 8) is squarely in the range Gilbert and co-workers report for fusion first-wall steels on a $14\,MeV$ spectrum (order 10–$15\,appm/dpa$ for RAFM) [4,6], and roughly $40\times$ the value a fast reactor delivers [17]. This is the quantitative form of the standard warning that fission-irradiation data cannot be transferred to fusion without a helium correction [16,15]: at fixed dpa the fusion wall carries an order of magnitude more helium, and it is helium that stabilises voids and embrittles grain boundaries. Our swelling result must be read in that light — and it is reassuring that even at the fusion He/dpa the bubbles remain in the sub-percent, dense-equilibrium regime.

SWELLING IN THE DENSE-BUBBLE REGIME

The swelling values (0.024% W, 0.017% RAFM) sit inside the literature band for tungsten and ferritic steel at ~ 10–20 dpa and hundreds of appm helium [18,16], and well below the onset of the void-swelling regime that afflicts austenitic steels. The physical reason the result is robust is the equilibrium-bubble closure (equation 9): in the dense-gas limit swelling depends on the total gas content and only weakly on the nucleation density, so the order-of-magnitude uncertainty in n_b from the reduced-order model does not propagate to the swelling. Trinkaus's high-pressure bubble equation of state [14] and Ghoniem's rate theory [13] underlie this closure; the pending high-fidelity Xolotl run [29] is the designated arbiter for the nucleation density and any vacancy-void augmentation.

SPUTTERING AND PERMEATION IN CONTEXT

The peak D→W physical sputter yield of 1.35×10^{-2} atoms ion^{-1} agrees with the calibrated Eckstein/Bohdansky database [21,22] and with the canonical $\sim 10^{-2}$ value for keV deuterium on tungsten; the tungsten choice itself is motivated by its high sputter threshold and low retention [18,25,7]. The steady tritium permeation flux ($\approx 0.56\%$ of the implanted flux) and the minutes-scale breakthrough lag are consistent with diffusion-limited permeation through a tungsten-fronted stack given tungsten's low hydrogen diffusivity and solubility [27], and the finite-element solution reproduces the analytic two-layer steady flux to seven significant figures [26,28]. The one caveat the literature demands — that neutron-induced traps can raise the *retained* inventory by one to two orders of magnitude even where they leave the steady flux unchanged — is carried explicitly to the barrier-coating and safety companions [42].

§ 6

Limitations

Three honest caveats bound the claims, and one is the governing open item. First and foremost, the tungsten damage channel presently uses an elastic-only recoil gap-filler: SPECTRA-PKA ships Fe-56 and Zr recoil matrices but no tungsten set, and the NJOY21 tungsten recoil matrices were not yet generated locally, so the W PKA spectrum is derived from ENDF/B-VIII.0 MF4 elastic angular data folded with the armor-transmitted flux rather than from a full **79**-channel recoil matrix. This affects the tungsten *armor* damage and helium numbers; the load-bearing structural rate $9.78\,dpa/fpy$ is computed on the complete Fe-56 channel set and is unaffected. Generating the tungsten recoil matrices (a TENDL-PKA download plus an NJOY21 run) is the designated follow-on that closes this item. Second, the swelling result uses a reduced zero-dimensional van der Waals rate-theory model because the high-fidelity Xolotl spatial solver was disabled by a build-time library incompatibility; the dense-bubble closure makes the swelling robust, and a lattice-KMC model corroborates the regime, but the high-fidelity Xolotl run remains the arbiter for nucleation density and vacancy-void augmentation. Third, the dpa-to-failure criterion uses conservative embrittlement limits (a damage budget of order **20** dpa) rather than a measured wall lifetime; the mechanical qualification that would replace the budget with measured strength, ductility and DBTT-shift data is the subject of the RAFM-steel qualification companion [37]. None of these caveats changes the ordering of equation (1): displacement embrittlement binds.

§ 7

Conclusion

The first wall of the Hyperion compact spherical-tokamak breeder is displacement-limited. On an independent, GPU-accelerated code stack driven by the frozen $14\,MeV$ source term, the RAFM structure behind $3\,mm$ of tungsten armor accumulates displacement damage at $9.78\,dpa/fpy$ (bare-wall upper bound $18.85\,dpa/fpy$), reaching the replacement-class budget of order 20 dpa in a service interval of about two full-power-years. The three other channels are quantified and subdominant: transmutation helium co-produces at $\approx 12\,appm/dpa$ — an order of magnitude above any fission spectrum, and the reason the lifetime must be set on the fusion spectrum — yet drives only 0.024% (tungsten) and 0.017% (RAFM) swelling in the dense-equilibrium-bubble regime, more than an order of magnitude below the design limit; physical sputtering of the armor peaks at 1.35×10^{-2} atoms ion^{-1} and removes sub-monolayer material per pulse; and tritium permeation, at $5.16e14\,/m^2s$ ($\approx 0.56\%$ of the implanted flux), is a fuel-cycle and safety boundary condition rather than a wall clock. The wall is a scheduled-replacement component on a defined damage budget — the survival question answered directly, and distinctly from the activation and waste classification. Every headline quantity is a frozen anchor (BR-L2-A24 through BR-L2-A27) in the Kronos de-risking register, and the one open engineering item — a full tungsten recoil-matrix damage run — is a defined, bounded follow-on.

Acknowledgments tocsectionAcknowledgments Part of the Kronos Fusion Energy 2026 design series. The authors thank the Kronos physics de-risking programme for the frozen result set underlying every quantitative claim, and the operators of the NVIDIA GPU HPC campaign for the cascade and transport runs.

Reproducibility. Every headline quantity in this paper is a frozen anchor (BR-L2-A24, BR-L2-A25, BR-L2-A26, BR-L2-A27) in the Kronos Physics De-Risking Register [35] (doi:10.5281/zenodo.22133057) and is regenerable from the seed-pinned, version-locked gate cards; this paper is archived at doi:10.5281/zenodo.22645774; official version: https://www.kronosfusionenergy.com/publications/first-wall-neutron-damage-lifetime.html. The figures are regenerated by the deposited script `make_fw230_figs.py` from the frozen register values. No result depends on unpublished or proprietary data, and no compute-cost information is part of the public deposit.

Data availability tocsectionData availability The displacement-damage, transmutation-gas, swelling, sputter-yield and permeation values used for figures 3–8 are frozen anchors (gates BR-L2-A24–A27) in the register [35] and are archived with this paper at doi:10.5281/zenodo.22645774. No economics is included in the public deposit.

Competing interests tocsectionCompeting interests Provisional patent applications relating to aspects of this work have been filed.

tocsectionReferences

APPARATUS

Portfolio, People & Record

The intellectual-property estate, the people who built it, the limitations that gate it, and the sources it rests on.

1	4	40	27
GRANTED PATENT	2026 PROVISIONALS	TEAM MEMBERS	2022 PROVISIONALS

INTELLECTUAL PROPERTY

The patent portfolio

The estate spans a granted high-field magnet patent, pending utility and 2026 provisional filings that map to the two products, a digital-twin control provisional, a registered trademark application, and the original 2022 provisional family. Every patentable disclosure in the five-paper arXiv drop was protected **before** publication: the breeder and burner provisionals were filed 1–2 August, and a publication-gap omnibus filing the evening before the drop swept up the DEC, plasma-control, and REBCO-winding matter of the three otherwise-unprotected papers. Patent numbers and application serials are matters of public record; claim scope is summarised, not reproduced.

GRANTED & PENDING UTILITY

US 12,009,112	High-field tilted graded-REBCO magnet architecture (KRONO-002A) · *app. 17/878,550*	GRANTED
US 17/878,507	Core device / method (KRONO-001A) · *utility*	PENDING

2026 PROVISIONAL FILINGS — MAPPED TO THE PRODUCTS

64/124,209	Hyperion — spherical-tokamak tritium / helium-3 foundry · *breeder · filed Aug 2026*	FILED
64/124,220	Aegis / MetroVolt — synchrotron-cutoff, fuel-selection & plug-winding · *generator · filed Aug 2026*	FILED
64/115,167	KRONOS-CTRL digital-twin plant control · *provisional · filed Jul 2026*	FILED
64/005,440	Integrated spherical-tokamak fusion architecture · *early integrated-architecture filing · filed Mar 2026*	FILED
64/105,530	Negative-triangularity spherical-tokamak architecture · *foundational ST filing · filed Jul 2026*	FILED
64/128,097	Publication-gap omnibus — quasineutral two-species expander DEC · provenance-gated / latency-split plasma control · as-built high-field winding & conductor architecture · *filed 7 Aug 2026, the evening before the arXiv drop*	FILED

TRADEMARK & ORIGIN

FTK-98801894	Kronos Fusion Energy — trademark application	FILED
KR-2022-*	Original provisional family (KR-2022-00001 … 00027) · *27 filings, 2022*	PRIORITY

The narrow, defensible magnet novelty — the specific conductor and the digital-twin winding optimisation, not high-field REBCO as a category — is the commercial core that can earn ahead of any Q > 1 milestone, with markets in fusion magnet supply, MRI/NMR, accelerators, and proton therapy. The claim is scoped honestly: the high field is a *system field* result, not a stand-alone-coil record; the small-bore plug coil is structurally infeasible as a bare winding but resolved by a stress-managed structural shield (feasible-pending-FEA); and the winding-tape experiment returned a *null result*. The value is the method, not a field record.

THE TEAM

Founding partners, board, advisors & auditors

Kronos is built by a bench of advanced-fuel-fusion, high-field-magnet, direct-conversion, and materials specialists, with a board and operations team drawn from defense, national laboratories, and industry. Dates are shown as ranges; where a tenure has ended or is term-ending, the range says so.

FOUNDING PARTNERS — SCIENCE

Dr. Gerald Kulcinski
Co-Founder · Helium-3 & Advanced-Fuel Fusion
UW–Madison · 2023–Present

Dr. Carl Weggel
Chief Scientist / S.M.A.R.T. Design
MIT Alcator Program · 2022–Present

Dr. Robert J. Weggel
Magnetic Field Design
MIT Magnet Lab · 2022–Present

BOARD

Priyanca Ford
Founder & CEO · Executive Board
2022–Present

Bandel Carano
Finance / Strategy
Oak Investment Partners / Stanford · 2025–2026

Patrick Schweiger
Fusion Device Engineering
Oklo / CFS / TerraPower · 2025–Present

SCIENTIFIC ADVISORS

Dr. Steven O. Dean
Fusion Policy & History
DOE / Fusion Power Associates · 2025–Present

Dr. Patrick H. Diamond
Plasma Turbulence & Transport
UC San Diego · 2025–Present

Dr. Jack J. Dongarra
HPC & Numerical Algorithms
Turing Award · 2025–Present

Dr. Nasr M. Ghoniem
Chief Material Scientist
UCLA · 2025–Present

Dr. Siegfried Glenzer
Plasma Physics & Laser Fusion
Stanford / SLAC · 2022–Present

Dr. David A. Hammer
Pulsed-Power Fusion
Cornell · 2025–Present

Dr. Donald A. Spong
Plasma Theory & Confinement
ORNL · 2025–Present

Dr. Curtis Smith
Risk Assessment & Nuclear PRA
MIT / Idaho National Lab · 2025–Present

RADM (Ret.) David Goggins
Naval Engineering & Power-Plant Design
U.S. Navy · 2023–2026

Dr. Konstantin Batygin
Mathematician
Caltech · 2022–2025

Dr. Ruben Fair
Magnet Design / ITER Liaison
PPPL / Jefferson Lab · 2022–2025

Dr. Paul S. Weiss
Materials & Nanotechnology
UCLA · 2022–2025

SCIENTIFIC AUDITORS

Dr. Wilfred A. Cooper
Plasma Equilibrium Theory
EPFL / Swiss Plasma Center · 2025–Present

Dr. Ahmed Hassanein
Plasma–Material Interactions
Purdue / Argonne · 2025–Present

Dr. Patrick E. Hopkins
Extreme Thermal Materials
U. of Virginia · 2025–Present

Dr. Peter Hosemann
Materials Joining & Structural Integrity
UC Berkeley · 2025–Present

Dr. Travis W. Knight
Advanced Nuclear Fuels & Systems
U. of South Carolina · 2025–Present

Dr. Philippe Lebrun
Cryogenics & Magnet Cooling
CERN · 2025–Present

Dr. Nitendra Singh
Nuclear Safety & Fuel Cycle
ITER · 2025–Present

Dr. Guido Van Oost
Magnetic Confinement & Fusion Systems
Ghent University · 2025–Present

Dr. Gary S. Was
Radiation Materials & Structural Integrity
U. of Michigan · 2025–Present

Dr. Ray Sedwick
Direct Energy Conversion
U. of Maryland · 2025

OPERATIONS

Michael Laughlin
Chief Operating Officer
2022–Present

Martin Owens
Chief Strategy Officer
LANL / GE Hitachi · 2022–Present

MG (Ret.) Paul Pardew
Chief Contracting Officer
Army Contracting Command · 2022–Present

David Beck
Fusion Commercialization
U.S. Space Force · 2024–Present

Sushma Bhatia
Environmental & Legislative
Google · 2022–Present

Michael De Frenza
Technology Licensing
2023–Present

MG (Ret.) Robin L. Fontes
Cybersecurity & Defense
Army Cyber Command · 2022–Present

Vijay Gehani
Supply Chain & Components
INOX India · 2024–Present

Jon Michel Greenwood
IT & AI Infrastructure
Live Nation · 2023–Present

Brian C. O'Neill
National Security
CIA / ODNI · 2022–Present

Gen. (Ret.) Gustave F. Perna
DoD Liaison
Operation Warp Speed · 2022–2023

Andrea Romero
Marketing Lead
2022–Present

Legal counsel is retained; those roles are held on the internal roster and are not listed here.

SOURCES

References

1 M J Norgett, M T Robinson and I M Torrens, A proposed method of calculating displacement dose rates, *Nucl. Eng. Des.* **33** 50 (1975). doi:10.1016/0029-5493(75)90035-7

2 K Nordlund *et al*, Improving atomic displacement and replacement calculations with physically realistic damage models, *Nat. Commun.* **9** 1084 (2018). doi:10.1038/s41467-018-03415-5

3 K Nordlund *et al*, Primary radiation damage: A review of current understanding and models, *J. Nucl. Mater.* **512** 450 (2018). doi:10.1016/j.jnucmat.2018.10.027

4 M R Gilbert *et al*, Neutron-induced dpa, transmutation, gas production, and helium embrittlement of fusion materials, *J. Nucl. Mater.* **442** S755 (2013). doi:10.1016/j.jnucmat.2013.03.085

5 M R Gilbert, S L Dudarev, S Zheng, L W Packer and J-Ch Sublet, An integrated model for materials in a fusion power plant: transmutation, gas production, and helium embrittlement under neutron irradiation, *Nucl. Fusion* **52** 083019 (2012). doi:10.1088/0029-5515/52/8/083019

6 M R Gilbert, J-Ch Sublet and S L Dudarev, Spatial heterogeneity of tungsten transmutation in a fusion device, *Nucl. Fusion* **57** 044002 (2017).

7 J Marian *et al*, Recent advances in modeling and simulation of the exposure and response of tungsten to fusion energy conditions, *Nucl. Fusion* **57** 092008 (2017). doi:10.1088/1741-4326/aa5e8d

8 M R Gilbert and J-Ch Sublet, SPECTRA-PKA: primary-knock-on-atom spectra from processed nuclear data for radiation-damage analysis, *Culham Centre for Fusion Energy* (software and methodology), UK Atomic Energy Authority.

9 R E MacFarlane, D W Muir, R M Boicourt, A C Kahler and J L Conlin, The NJOY nuclear data processing system, version 2016, *Los Alamos National Laboratory* LA-UR-17-20093 (2017).

10 D A Brown *et al*, ENDF/B-VIII.0: The 8th major release of the nuclear reaction data library, *Nucl. Data Sheets* **148** 1 (2018). doi:10.1016/j.nds.2018.02.001

11 A J Koning, D Rochman, J-Ch Sublet, N Dzysiuk, M Fleming and S van der Marck, TENDL: complete nuclear data library for innovative nuclear science and technology, *Nucl. Data Sheets* **155** 1 (2019). doi:10.1016/j.nds.2019.01.002

12 A P Thompson *et al*, LAMMPS – a flexible simulation tool for particle-based materials modeling at the atomic, meso, and continuum scales, *Comput. Phys. Commun.* **271** 108171 (2022). doi:10.1016/j.cpc.2021.108171

13 N M Ghoniem and G L Kulcinski, A critical assessment of the effects of pulsed irradiation on the microstructure, swelling and creep of materials, *Nucl. Eng. Des./Fusion* **1** 373 (1984).

14 H Trinkaus, Energetics and formation kinetics of helium bubbles in metals, *Radiat. Eff.* **78** 189 (1983).

15 H Ullmaier, The influence of helium on the bulk properties of fusion reactor structural materials, *Nucl. Fusion* **24** 1039 (1984).

16 S J Zinkle and G S Was, Materials challenges in nuclear energy, *Acta Mater.* **61** 735 (2013). doi:10.1016/j.actamat.2012.11.004

17 G S Was, *Fundamentals of Radiation Materials Science: Metals and Alloys*, 2nd ed., Springer, New York (2017).

18 M Rieth *et al*, Recent progress in research on tungsten materials for nuclear fusion applications in Europe, *J. Nucl. Mater.* **432** 482 (2013). doi:10.1016/j.jnucmat.2012.08.018

19 R Lindau *et al*, Present development status of EUROFER and ODS-EUROFER for application in blanket concepts, *Fusion Eng. Des.* **75–79** 989 (2005).

20 P Sigmund, Theory of sputtering. I. Sputtering yield of amorphous and polycrystalline targets, *Phys. Rev.* **184** 383 (1969). doi:10.1103/PhysRev.184.383

21 J Bohdansky, A universal relation for the sputtering yield of monatomic solids at normal ion incidence, *Nucl. Instrum. Methods B* **2** 587 (1984).

22 W Eckstein, Sputtering yields, in *Sputtering by Particle Bombardment* (ed. R Behrisch and W Eckstein), Topics in Applied Physics **110** 33, Springer (2007).

23 J T Drobny and D Curreli, RustBCA: A high-performance binary-collision-approximation code for ion-material interactions, *J. Open Source Softw.* **6** 3298 (2021).

24 J F Ziegler, M D Ziegler and J P Biersack, SRIM – The stopping and range of ions in matter (2010), *Nucl. Instrum. Methods B* **268** 1818 (2010). doi:10.1016/j.nimb.2010.02.091

25 G Federici *et al*, Plasma-material interactions in current tokamaks and their implications for next step fusion reactors, *Nucl. Fusion* **41** 1967 (2001).

26 A McNabb and P K Foster, A new analysis of the diffusion of hydrogen in iron and ferritic steels, *Trans. Metall. Soc. AIME* **227** 618 (1963).

27 R Frauenfelder, Solution and diffusion of hydrogen in tungsten, *J. Vac. Sci. Technol.* **6** 388 (1969).

28 R Delaporte-Mathurin, E A Hodille, J Mougenot, Y Charles and C Grisolia, Finite element analysis of hydrogen retention in ITER plasma facing components using FESTIM, *Nucl. Mater. Energy* **21** 100709 (2019). doi:10.1016/j.nme.2019.100709

29 S Blondel, D E Bernholdt, K D Hammond and B D Wirth, Continuum-scale modeling of helium bubble bursting under plasma-exposed tungsten surfaces, *Nucl. Fusion* **58** 126034 (2018).

30 S Plimpton, C Battaile, M Chandross *et al*, Crossing the mesoscale no-man's land via parallel kinetic Monte Carlo (SPPARKS), *Sandia National Laboratories* SAND2009-6226 (2009).

31 P K Romano, N E Horelik, B R Herman, A G Nelson, B Forget and K Smith, OpenMC: A state-of-the-art Monte Carlo code for research and development, *Ann. Nucl. Energy* **82** 90 (2015). doi:10.1016/j.anucene.2014.07.048

32 J E Menard *et al*, Fusion nuclear science facilities and pilot plants based on the spherical tokamak, *Nucl. Fusion* **56** 106023 (2016). doi:10.1088/0029-5515/56/10/106023

33 B N Sorbom *et al*, ARC: a compact, high-field, fusion nuclear science facility and demonstration power plant with demountable magnets, *Fusion Eng. Des.* **100** 378 (2015). doi:10.1016/j.fusengdes.2015.07.008

34 G Federici *et al*, Overview of the DEMO staged design approach in Europe, *Nucl. Fusion* **59** 066013 (2019). doi:10.1088/1741-4326/ab1178

35 P I Ford, *KRONOS Physics De-Risking Register*, v8, Kronos Fusion Energy 2026 series. doi:10.5281/zenodo.22133057

36 P I Ford and G L Kulcinski, *Plasma-material interaction in a compact spherical-tokamak breeder: sputtering, net erosion, and redeposition setting the plasma-facing-surface lifetime*, Kronos Fusion Energy 2026 series. doi:10.5281/zenodo.22645885

37 P I Ford and G L Kulcinski, *Qualifying reduced-activation ferritic-martensitic steel for a compact spherical-tokamak breeder: strength, DBTT shift and swelling under 14 MeV neutron loading*, Kronos Fusion Energy 2026 series. doi:10.5281/zenodo.22645887

38 P I Ford and G L Kulcinski, *First-wall thermomechanics and fatigue life of plasma-facing components under combined surface and volumetric loading in a compact spherical-tokamak breeder*, Kronos Fusion Energy 2026 series. doi:10.5281/zenodo.22645850

39 P I Ford and G L Kulcinski, *Component activation, waste-class routing, and decommissioning of a low-activation compact spherical-tokamak breeder*, Kronos Fusion Energy 2026 series. doi:10.5281/zenodo.22645846

40 P I Ford and G L Kulcinski, *CAD-faithful neutronics for a compact spherical-tokamak breeder: STEP-to-DAGMC Monte-Carlo transport reproducing the 3-D net tritium-breeding ratio*, Kronos Fusion Energy 2026 series. doi:10.5281/zenodo.22645881

41 P I Ford, *Nuclear-data uncertainty quantification for tritium breeding: which 14 MeV cross-section channels set the error bar on the breeding ratio*, Kronos Fusion Energy 2026 series. doi:10.5281/zenodo.22645777

42 P I Ford and G L Kulcinski, *Tritium permeation-barrier coatings for a compact spherical-tokamak breeder: the liquid-lithium-over-tin wall-chemistry choice*, Kronos Fusion Energy 2026 series. doi:10.5281/zenodo.22645870

43 P I Ford, *Prognostics and remaining-useful-life estimation for the consumable centrepost: a dual-channel fluence-driven framework scheduling cartridge replacement*, Kronos Fusion Energy 2026 series. doi:10.5281/zenodo.22645788

COLOPHON

How this document was made

The Kronos Fleet — Combined Editorial, 2026 is set in **Fraunces** (display), **Gelasio** (text), and **IBM Plex Mono** (data & equations), carried forward from the Kronos editorial design system.

The figures are rendered at 300 dpi from the deposited generator scripts; the document is composed as a single self-contained file with embedded fonts and imagery, paginated to US Letter, and rendered to PDF through a headless Chromium engine in matched light and dark editions.

Every headline quantity carries an evidence class; withdrawn and restated values are marked as such. Nothing herein is frozen beyond the founder-approved Tier-A set.

Explore it live — turn the interactive 3-D model, run the deposited solvers in the physics validator, and watch the companion film series.

LEGAL NOTICE

Notice, status, and distribution

Conceptual design & simulation study. This document reports a conceptual design and simulation study. It is not a construction commitment, a safety-analysis report, a regulatory filing, or an offer of securities. Forward-looking statements — schedules, costs, market sizes, and performance — are estimates subject to the limitations set out in the Simulations part and may change.

Numbers and their classes. Quantities are reported with evidence classes and case labels; modelled, assumed, and requirement-class values are identified as such and are not to be quoted without their labels.

Public edition. This edition carries the physics and design only; all financial, funding, and defense-commercial content has been removed for public distribution. The scientific text corresponds to the arXiv and journal submissions.

THE 2026 KRONOS SERIES

One programme, many papers

This editorial is one paper in the Kronos 2026 series — a real fusion company's complete, reproducible physics record for a spherical-tokamak breeder and its low-neutron D–^{3}He tandem-mirror burners. Every headline number is a frozen anchor in the Physics De-Risking Register.

Explore the whole programme: the De-Risking Register, the interactive 3-D model, and the physics validator.

KRONOS FUSION ENERGY

First-Wall and Plasma-Facing-Component Lifetime Under 14 MeV Loading: Displacement Damage, Bubble Swelling and Erosion in a Compact Spherical-Tokamak Breeder

A real fusion company building real machines. Explore the science, live.

Zenodo · doi:10.5281/zenodo.22645774

Read on kronosfusionenergy.com

The Physics De-Risking Register